Microstructure and Charge–Discharge Mechanism of a Li_3CuS_2 Positive Electrode Material for All-Solid-State Lithium-Ion Batteries

Microstructure and charge–discharge mechanism of a Li_3CuS_2 positive electrode material for all-solid-state lithium-ion batteries

Tomoji Ayama[1], Hirofumi Tsukasaki[1], Yusuke Kawasaki[2], Hiroshi Nakajima[1], Masahiro Tatsumisago[2], Atsushi Sakuda[2], Akitoshi Hayashi[2], Shigeo Mori[1]*

[1]Department of Material Science, Graduate School of Engineering, Osaka Prefecture University, Osaka 599-8531, Japan

[2]Department of Applied Chemistry, Graduate School of Engineering, Osaka Prefecture University, Osaka 599-8531, Japan

KEYWORDS: all-solid-state lithium batteries, Li_2S, transmission electron microscopy, particle size distribution, Li_3CuS_2

ABSTRACT: To develop all-solid-state lithium batteries, high-capacity positive electrode materials are necessary. An antifluorite-type material, Li_2S, exhibits a high theoretical capacity. However, Li_2S cannot be used as a positive electrode for the all-solid-state cell because of the insulating behavior. To provide electronic and ionic conduction, recently, antifluorite-type

Li_3CuS_2 has been developed by activation of Li_2S by Cu substitution. Li_3CuS_2 is a favorable candidate for positive electrodes as sulfide-based all-solid-state cells with Li_3CuS_2 exhibit high charge–discharge performance. However, structural changes and redox species during charge–discharge cycle have not been understood yet. To clarify the charge–discharge mechanism of Li_3CuS_2, in this study, we examined the microstructural changes in a Li_3CuS_2–Li_3PS_4 positive electrode composite during charge and discharge by transmission electron microscopy (TEM). Hollow-corn dark-field imaging technique was employed to evaluate the crystallite size distribution. The result shows that the crystallite size of Li_3CuS_2 reversibly decreases and increases in the charging and discharging state, respectively. The electron diffraction pattern shows that $LiCuS_2$ was formed during charging, which is attributed to Li^+ extraction from Li_3CuS_2. In the discharging state, the crystallite size increased and Li_3CuS_2 was reproduced. The TEM results suggest that the reversible structural changes ($Li_3CuS_2 \leftrightarrows LiCuS_2 + 2Li^+ + 2e^-$) would contribute to high charge-discharge characteristics.

1. Introduction

Owing to their high charge–discharge properties and energy density, lithium-ion batteries are widely applied to electronic devices as an energy storage [1]. However, flammable organic electrolytes are commonly used in such batteries, which pose a safety concern. To resolve the safety concerns, all-solid-state batteries, which use incombustible inorganic solid electrolytes, have recently become the focus of attention [2–4].

The main advantage of all-solid-state cells is that several active materials can be introduced into the electrode layer, which leads to a further increase in energy density. Hence, to fabricate all-

solid-state cells, electrode active materials with high capacity are indispensable. For example, metal sulfides such as Li_2TiS_3, Li_3NbS_4, and Li_2FeS_2 have been employed as a positive electrode active material for all-solid-state cells [5–7]. Among many electrode active materials, in particular, Li_2S with an antifluorite-type structure exhibits high theoretical capacity (1167 mAh g^{-1}). However, Li_2S is an insulator; hence, there is a need to construct an electronic and ionic conduction path. Kawasaki et al. synthesized a new antifluorite-type positive electrode material, Li_3CuS_2, by partially substituting Cu^+ in the Li_2S with Li^+ [8]. Since Li_2S is activated by Cu substitution, electronic and ionic conduction can be achieved. Theoretical capacity of Li_3CuS_2 is approximately 540 mAh g^{-1}. They demonstrated that all-solid-state cells with electrode composites comprising of Li_3CuS_2 and Li_3PS_4 (LPS) glass exhibits high charge–discharge cycle performance and can operate without a conductive additive. In addition, their X-ray diffraction (XRD) measurements and *ex-situ* transmission electron microscopy (TEM) observations indicated that an antifluorite-type Li_3CuS_2 is regenerated after the initial discharge cycle [8]. However, reaction products during charging and redox species during charge–discharge cycles have not been clarified yet.

To reveal the charge–discharge mechanisms of Li_3CuS_2, in this study, the microstructural and morphological changes during long-term charge–discharge cycles of Li_3CuS_2–LPS positive electrode composites were investigated mainly by TEM. To quantitatively evaluate the structural changes during charge–discharge cycles, the crystallite size distribution was also analyzed using the hollow-corn dark-field (HCDF) imaging technique. Reaction products and redox species were examined by electron diffraction (ED) patterns and X-ray photoelectron spectroscopy. Based on the experimental results obtained, the charge–discharge mechanism of Li_3CuS_2 is discussed.

2. Materials and Methods

2.1. Preparation of all-solid-state cell

Li_3CuS_2 and LPS glasses were synthesized using the mechanochemical technique. These preparation procedures and mechanochemical conditions are described in our previous paper [8]. The positive electrode composite was prepared from Li_3CuS_2 and LPS glasses at a weight ratio of 70:30. Li-In alloy and LPS glasses were used as a negative electrode and an electrolyte layer, respectively. The detailed fabrication process and electrochemical measurement condition of all-solid-state cells (Li–In/LPS/Li_3CuS_2–LPS) have already been provided in our previous study [8].

2.2. Characterization

XRD measurements were conducted utilizing Cu Kα radiation and an X-ray diffractometer (SmartLab, Rigaku). XRD profiles were obtained in steps of 0.02° over the 2θ range of 10–80°. Scanning rate was 10 min^{-1}. To prevent air exposure, an airtight container was used during the XRD measurements. The electronic structure was analyzed by X-ray photoelectron spectroscopy (XPS, K-Alpha, Thermo Fisher Scientific) with a monochromatic Al Kα source (1486.6 eV).

2.3. TEM observation

Ex-situ TEM observations were performed utilizing a JEM-2100F field-emission TEM with a 14-bit CCD camera. Since Li_3CuS_2 and LPS are not stable in air, a double-tilt vacuum transfer TEM holder (Gatan model 648) was used. After charge−discharge tests, the cells were disassembled and the Li_3CuS_2–LPS positive electrode composites were removed. The composite powder was then mounted on a Cu grid for the TEM observation under an inert Ar atmosphere in a glove box. The morphology and microstructure of the composites were investigated by ED patterns and HCDF imaging. HCDF images are taken using the electron beam, which is tilted at a fixed angle and

automatically rotated with respect to the optical axis of the objective lens [9, 10]. Thus, diffraction spots and Debye–Scherrer rings in the ED pattern can be properly reflected onto the image as a bright contrast [11–16]. Taking advantage of this merit of HCDF imaging, we further analyzed the crystallite size distribution. As shown in Fig. 1(a), HCDF imaging could visualize the crystallites and spatial distribution as bright. Based on several HCDF images, each bright region is segmented as a crystallite by machine learning [17, 18], as indicated in red (Fig. 1(b)). Then, the crystallite size distribution could be represented in a histogram and the average crystallite diameters (*d*) were calculated. The crystalline phase was examined using the "ProcessDiffraction" software for the analysis of ED patterns [19, 20].

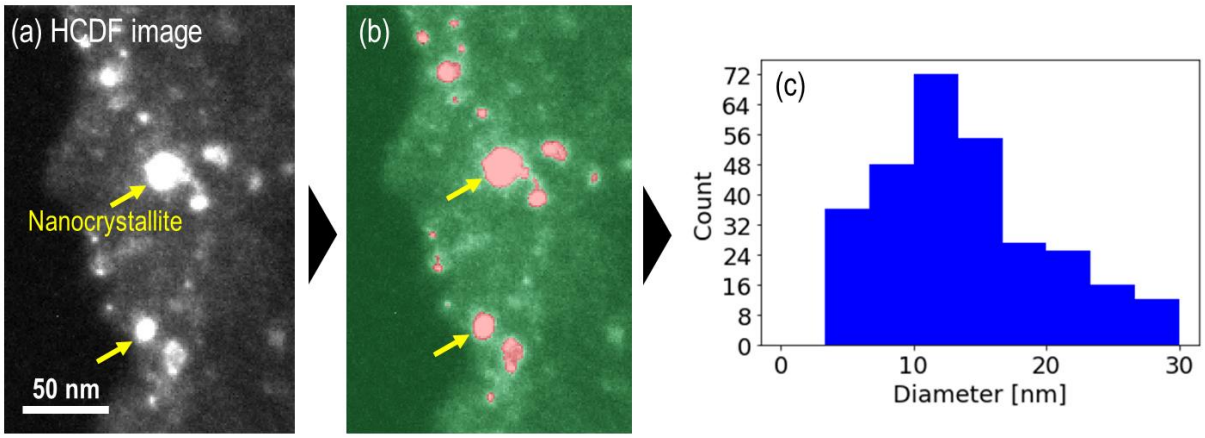

Figure 1. Crystallite size distribution analysis by HCDF imaging. (a) Original HCDF image. (b) HCDF image with the crystallites marked in red. (c) Histogram of the crystallite size distribution.

3. Results and discussion

The charge–discharge performance of the fabricated all-solid-state cells (Li–In/LPS/Li_3CuS_2–LPS) during long-term cycling was reported in our previous study [8]. The Li_3CuS_2 active material exhibited an initial charge and discharge capacity of 389 and 376 mAh g^{-1}, respectively. The

reversible capacity of 376 mAh g^{-1} is approximately equivalent to a two-electron reaction. In addition, the discharge capacity retention after the 40th cycle was approximately 88.2%. These results suggest high reversibility of Li_3CuS_2 and high cycle performance of the fabricated cells. Thus, to clarify the structural changes during long-term cycling, herein, we examined the morphology and microstructure of the Li_3CuS_2–LPS composites before and after the 1st and 15th charge–discharge cycles. Charge–discharge properties of the fabricated cell in the present study are shown in Fig. S1. Cycle stability of the present cell is almost the same as that reported in our previous study [8]. Fig. 2 shows the XRD pattern of the Li_3CuS_2–LPS composite before and after the 1st and 15th charge–discharge cycles. The pristine sample showed diffraction peaks ascribed to the antifluorite-type Li_3CuS_2 structure, as indicated by dotted lines. The intensities of these diffraction peaks significantly decreased in the charging state. Unknown diffraction peaks were also observed, as indicated by diamond shapes. In the discharging state, diffraction peaks for Li_3CuS_2 reappeared. That is, the antifluorite-type Li_3CuS_2 structure was reproduced. To further understand the charging state, the microstructure and morphology were investigated by *ex situ* TEM observations.

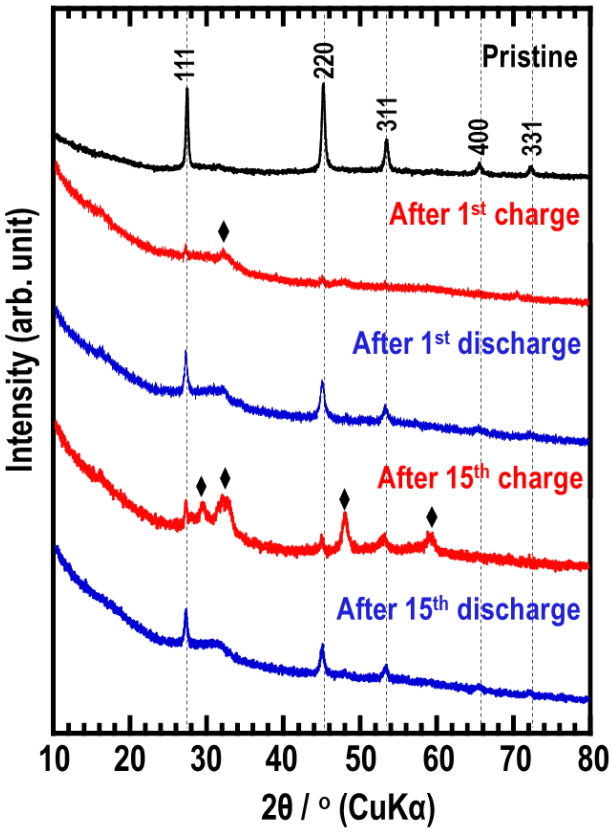

Figure 2. *Ex situ* XRD patterns of the Li_3CuS_2–LPS composite before and after the 1st and 15th charge–discharge process.

To clarify the morphological changes during long-term charge–discharge cycles, the crystallite size distribution was analyzed by HCDF imaging. Fig. 3 shows the HCDF images and histograms of the nanocrystallite size distribution before and after the 1st and 15th charge–discharge process. The histograms were derived from several areas of multiple HCDF images to increase the crystallite number. A difference in nanocrytallite size was observed between the charging and discharging states. The average Li_3CuS_2 crystallite size in the pristine and discharging state was approximately 15 nm, whereas it was less than 10 nm in the charging state. As indicated by the bright areas in the HCDF images, the particle size after discharging was larger than that after

charging. These indicate a decrease in the crystalline size of Li_3CuS_2 and the formation of reaction products different from Li_3CuS_2 during charging.

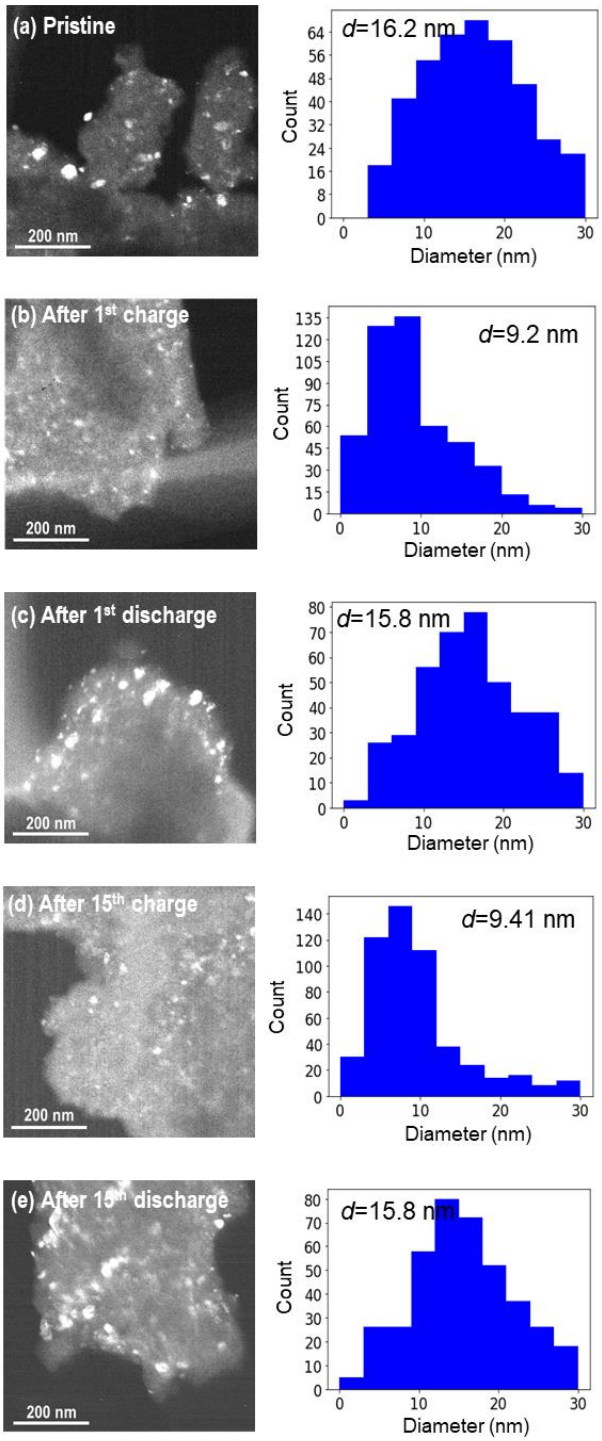

Figure 3. HCDF images and histograms of the nanocrystallite size distribution before and after the 1st and 15th charge–discharge process. The average crystallite size *d* is shown in each

histogram. (a) Pristine. (b) After the 1st charge. (c) After the 1st discharge. (d) After the 15th charge. (e) After the 15th discharge.

To verify the microstructure of Li_3CuS_2–LPS composite in the charging state, we obtained the ED patterns before and after the 1st and 15th charge–discharge process (Fig. 4). After the 1st and 15th discharging cycles, high-intensity Debye–Scherrer rings and diffraction spots were clearly observable, as shown in Fig. 4(c) and (e). The ED patterns are similar to that of the pristine sample (Fig. 4(a)). In contrast, after the 1st and 15th charging cycles, the intensity of the diffraction spots and Debye–Scherrer rings decreased and the ED patterns appeared different from that obtained after discharging, as shown in Fig. 4(b) and (d).

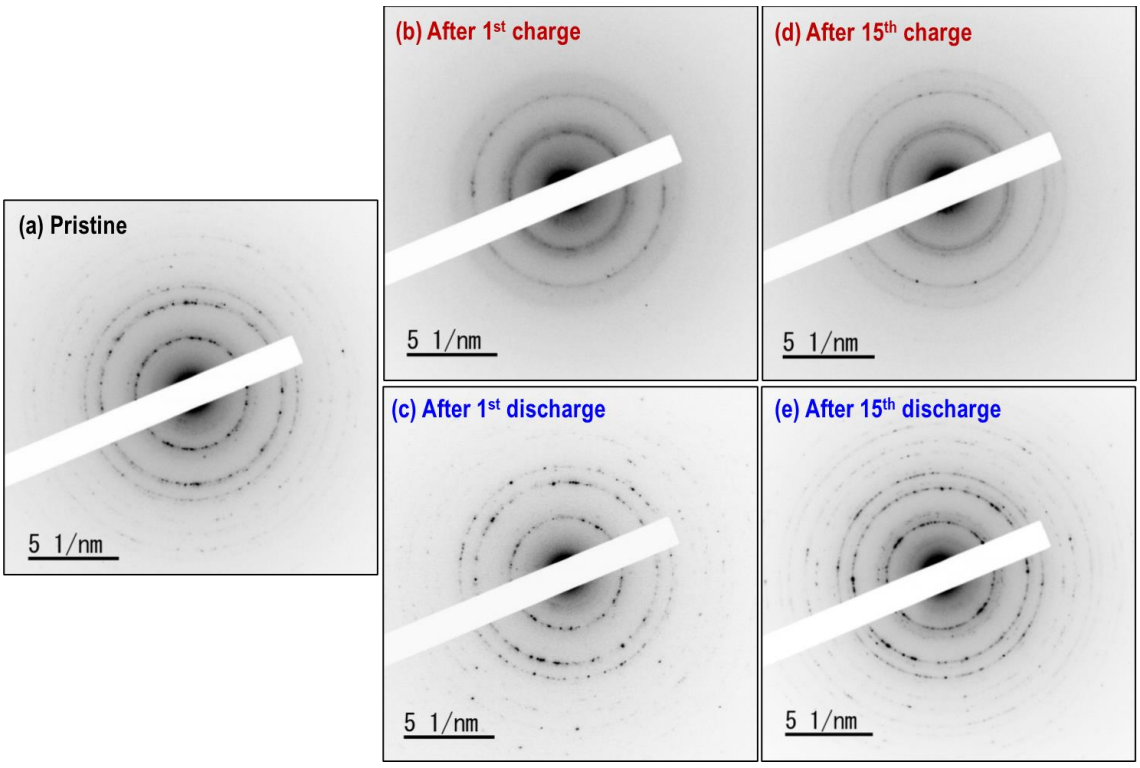

Figure 4. ED patterns of Li_3CuS_2 in the Li_3CuS_2–LPS composites before and after the 1st and 15th charge–discharge cycles. (a) Pristine. (b) After the 1st charge. (c) After the 1st discharge. (d) After the 15th charge. (e) After the 15th discharge.

Fig. 5 shows the intensity profiles obtained from each ED pattern in Fig. 4. Before and after the 1st and 15th discharging cycles, each diffraction peak was consistent with that of the simulated XRD pattern of antifluorite-type Li_3CuS_2, as shown in Fig. 5(a), (c), and (e). In contrast, after the 1st and 15th charging cycles, only peaks ascribed to $LiCuS_2$ were observed, as shown in Fig. 5(b) and (d).

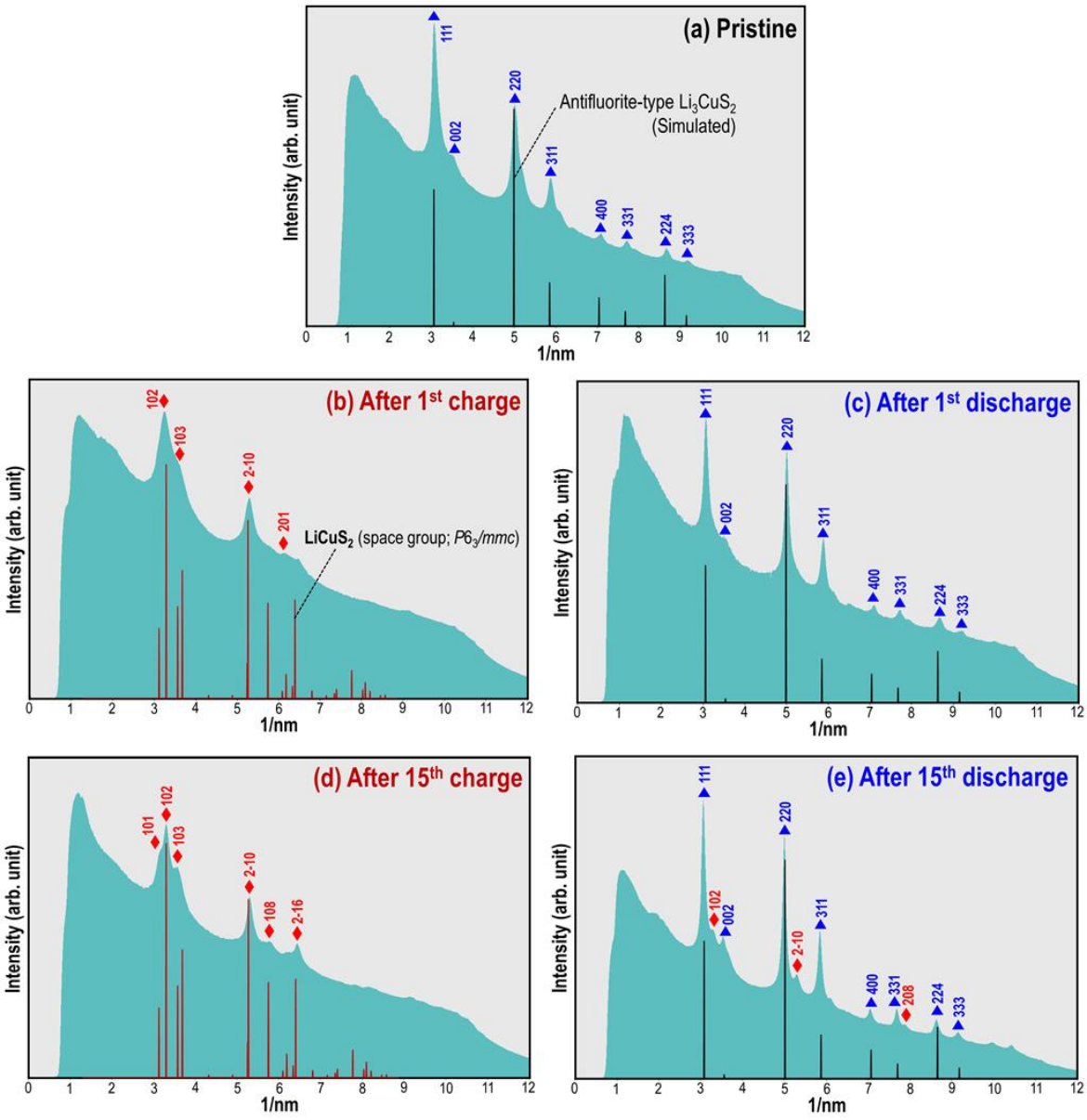

Figure 5. Intensity profiles corresponding to each ED pattern in Fig. 4. Blue triangles and red diamonds indicate the diffraction peaks of Li_3CuS_2 and $LiCuS_2$, respectively. (a) Pristine. (b) After the 1st charge. (c) After the 1st discharge. (d) After the 15th charge. (e) After the 15th discharge.

Fig. S2 of the Supplementary Information shows the crystal structure of $LiCuS_2$, as obtained using VESTA [17]. $LiCuS_2$ has the CuS structure (space group; $P6_3/mmc$), in which Cu occupies half of the cation site. Unknown peaks at 29.9°, 32.2°, 48°, and 59°, indicated by diamond shapes in Fig.

2, correspond to the 102, 103, $2\bar{1}0$, and $2\bar{1}6$ main diffraction peaks of $LiCuS_2$, respectively. After the 15th discharging cycle, the $LiCuS_2$, formed after the 15th cycle charging was partially retained. Fig. S3 (a) shows the S 2p XPS spectra of the Li_3CuS_2–LPS composites before and after the initial charge–discharge process. After the initial charging, a specific peak appeared on the high energy side, as indicated by the arrow. This suggests that the sulfide ions in Li_3CuS_2 were oxidized during charging. After the initial discharging, however, a spectrum similar to that before charging was obtained. This implies that sulfur underwent a reversible redox reaction during the charge–discharge process. Fig. S3(b) of the Supplementary Information shows the Cu 2p XPS spectra of the Li_3CuS_2–LPS composites before and after the initial charge–discharge process. There was no significant shift in peak during charging and discharging. To better understand the electronic state of Cu during charge–discharge cycles, there is a need for further investigation by other spectroscopic analysis techniques. $LiCuS_2$ with a CuS-type structure has S–S bonds. Thus, the XPS results support the attribution of the ED patterns after charging to $LiCuS_2$. It is inferred that $LiCuS_2$ was formed by Li^+ extraction from Li_3CuS_2 during charging.

Furthermore, the contribution of the LPS glass to the charge–discharge properties was examined. Fig. 6 shows the ED patterns of LPS before and after the 1st and 15th charge–discharge cycles. Since all the ED patterns exhibited a similar halo pattern, there were no significant structural changes in LPS during the charge–discharge. In addition, there was no shift in the main P 2p peak of LPS, as shown in Fig. S4. This suggests that the LPS glass was not mainly involved in the redox reaction.

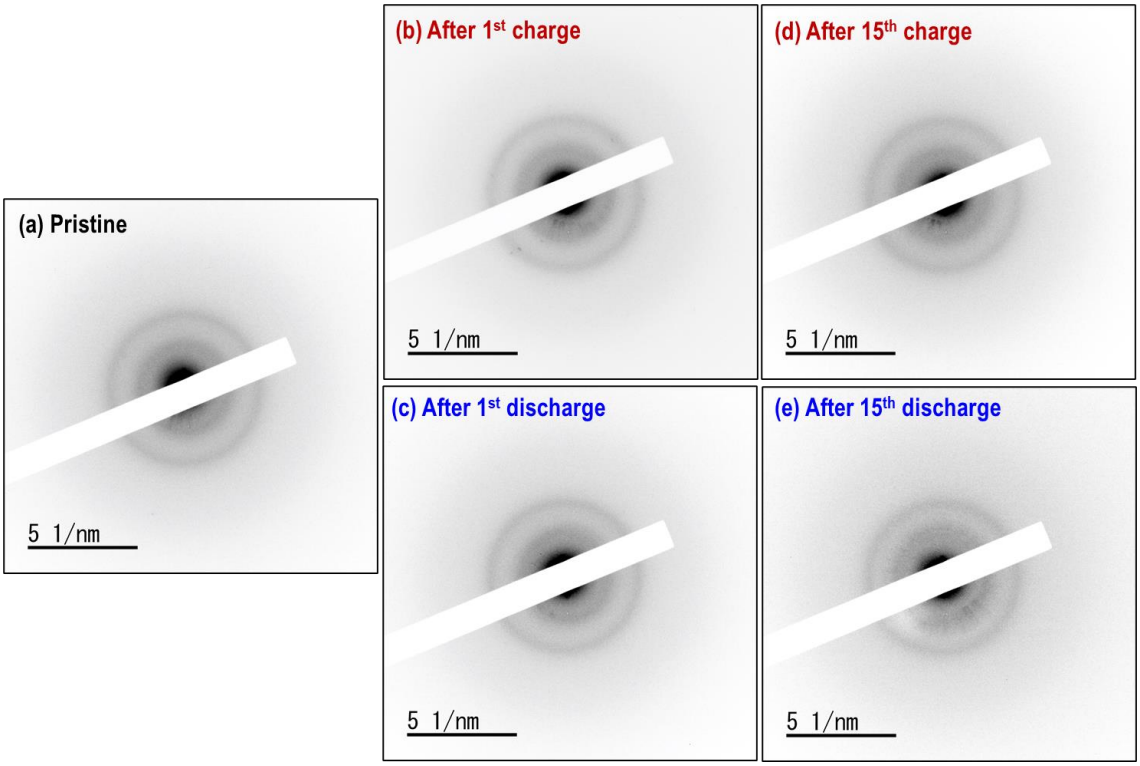

Figure 6. ED patterns of the LPS glass in the Li_3CuS_2–LPS composites before and after the 1st and 15th charge–discharge cycles. (a) Pristine. (b) After the 1st charge. (c) After the 1st discharge. (d) After the 15th charge. (e) After the 15th discharge.

The Li_3CuS_2–LPS positive electrode composites were analyzed by *ex situ* TEM to reveal the charge–discharge mechanism of Li_3CuS_2. From the morphology, the crystallite size of Li_3CuS_2 decreased during charging. The ED patterns revealed that the decrease in the crystallite size was a result of the formation of the $LiCuS_2$ crystalline phase. In the discharging state, the crystallite size returned to that of the pristine sample and the antifluorite-type Li_3CuS_2 structure was reproduced. This implies that the following reversible structural changes occurred during the charge–discharge cycles, which likely contributed to the high charge–discharge characteristics.

$$Li_3CuS_2 \leftrightarrows LiCuS_2 + 2Li^+ + 2e^-$$

After the 15th discharging cycle, the diffraction peaks attributed to the undischarged crystallites of $LiCuS_2$ were partially retained, as shown in Fig. 5(e). This suggests that as the number of undischarged $LiCuS_2$ nanocrystallites increases with an increase in cycle number, cycle performance deteriorates. To further improve the electron conduction path and charge–discharge cycle performance, it would be effective to include a conduction-promoting additive in the Li_3CuS_2–LPS composites.

4. Conclusions

To investigate the charge–discharge mechanism of Li_3CuS_2, we conducted *ex situ* TEM on a Li_3CuS_2–LPS positive electrode composite before and after long-term charge–discharge cycles. The crystallite size distribution was analyzed by HCDF imaging, which revealed that the Li_3CuS_2 crystallite size decreased during charging and was restored during discharging. The ED patterns show that the $LiCuS_2$ crystalline phase was formed in the charging state, whereas an antifluorite-type Li_3CuS_2 structure was regenerated in the discharging states. This indicates that Li_3CuS_2 gives off Li^+ during charging to form $LiCuS_2$. In other words, the reversible structural changes ($Li_3CuS_2 \leftrightarrows LiCuS_2 + 2Li^+ + 2e^-$) occur during the charge–discharge cycles, which could contribute to high cycle performance.

ASSOCIATED CONTENT

Supporting Information

The following files are available free of charge. Cycle performance of the cell, crystal structure of $LiCuS_2$, and XPS measurement results as presented in Figures S1−S4 (PDF).

Corresponding Author

*Hirofumi Tsukasaki

Department of Materials Science, Graduate School of Engineering, Osaka Prefecture University, 1-2, Gakuen-cho, Naka-ku, Sakai, Osaka 599-8570, Japan

Tel.: +81-72- 252-116; Fax.: +81-72-2549509

E-mail address: h-tsukasaki57@mtr.osakafu-u.ac.jp

Author Contributions

T.A. developed the idea. T.A., H.T., H.N., and S.M. conducted *ex situ* TEM observations. Crystallite size distribution was analyzed by T.A. and H.N. Y.K. prepared samples and performed XRD and XPS measurements. A.S., M.T., and A.H. supervised the project. All authors discussed the experimental results obtained. H.T. prepared the manuscript with input from all authors.

Notes

The authors declare no competing financial interest.

Acknowledgement

This work was supported by JST ALCA-SPRING (Grant JPMJAL1301), Japan. Also, this work was in part supported by JSPS KAKENHI Grant Number JP19H05814.

References

[1] Goodenough, J. B.; Kim, Y. Challenges for Rechargeable Li Batteries. *Chem. Mater.* 22 (2010)

587–603.

[2] Minami, T.; Hayashi, A.; Tatsumisago, M. Recent progress of glass and glass-ceramics as solid electrolytes for lithium secondary batteries. *Solid State Ionics* 177 (2006) 2715–2720.

[3] Kamaya, N.; Homma, K.; Yamakawa, Y.; Hirayama, M.; Kanno, R.; Yonemura, M.; Kamiyama, T.; Kato, Y.; Hama, S.; Kawamoto, K.; Mitsui, A. A lithium superionic conductor, *Nat. Mater.* 10 (2011) 682–686.

[4] Sakuda, A.; Hayashi, A.; Tatsumisago, M. Sulfide solid electrolyte with favorable mechanical property for all-solid-state lithium battery. *Sci. Rep.* 3 (2013) 2261.

[5] Sakuda, A.; Takeuchi, T.; Okamura, K.; Kobayashi, H.; Sakaebe, H.; Tatsumi, K.; Ogumi, Z. Rock-salt-type lithium metal sulphides as novel positive-electrode materials. *Sci. Rep.* 4 (2015) 4883.

[6] Sakuda, A.; Takeuchi, T.; Shikano, M.; Sakaebe, H.; Kobayashi, H. High reversibility of "soft" electrode Materials in all-solid-state Batteries. *Front. Energy Res.* 4(19) (2016) 00019.

[7] Takada, K.; Kitami, Y.; Inada, T.; Kajiyama, A.; Kouguchi, M.; Kondo, S.; Watanabe, M.; Tabuchi, M. Electrochemical Reduction of Li_2FeS_2 in Solid Electrolyte. *J. Electrochem. Soc.* 148 (2001) A1085.

[8] Kawasaki, Y.; Tsukasaki, H.; Ayama, T.; Mori, S.; Deguchi, M.; Tatsumisago, M.; Sakuda, A.; Hayashi, A. Synthesis and Electrochemical Properties of Li_3CuS_2 as a Positive Electrode Material for All-Solid-State Batteries, *ACS Appl. Energy Mater.* 4 (2021) 20−24.

[9] Yao, B.; Sun, T.; Warren, A.; Heinrich, H.; Barmak, K.; Coffey, K. R. High contrast hollow-cone dark field transmission electron microscopy for nanocrystalline grain size quantification, *Micron* 41 (2010) 177–182.

[10] Kulovits, A.K.; Facco, G.; Wiezorek, J.M.K. Grain size determination in nano-scale polycrystalline aggregates by precession illumination-hollow cone dark field imaging in the transmission electron microscope, *Mater. Charact.* 63 (2012) 17–26.

[11] Tsukasaki, H.; Mori, S.; Shiotani, S.; Yamamura, H. Ionic conductivity and crystallization process in the Li_2S–P_2S_5 glass electrolyte, *Solid State Ionics* 317 (2018) 122–126.

[12] Tsukasaki, H.; Otoyama, M.; Kimura, T.; Mori, S.; Sakuda, A.; Hayashi, A.; Tatsumisago, M. Exothermal behavior and microstructure of a $LiNi_{1/3}Mn_{1/3}Co_{1/3}O_2$ electrode layer using a Li_4SnS_4 solid electrolyte, *J. Power Sources* 479 (2020) 228827.

[13] Tsukasaki, H.; Morimoto, H.; Mori, S. Ionic conductivity and thermal stability of Li_2O–Li_2S–

P_2S_5 oxysulfide glass, *Solid State Ionics* 347 (2020) 115267.

[14] Tsukasaki, H.; Uchiyama, T.; Yamamoto, K.; Mori, S.; Uchimoto, Y.; Kowada, H.; Hayashi, A.; Tatsumisago, M. Exothermal mechanisms in the charged $LiNi_{1/3}Mn_{1/3}Co_{1/3}O_2$ electrode layers for sulfide-based all-solid-state lithium batteries, *J. Power Sources* 434 (2019) 226714.

[15] Tsukasaki, H.; Morimoto, H.; Mori, S. Thermal behavior and microstructure of the Li_3PS_4–ZnO composite electrolyte, *J. Power Sources* 436 (2019) 226865.

[16] Hikima, K.; Huy Phuc, N.H.; Tsukasaki, H.; Mori, S.; Muto, H.; Matsuda, A. High ionic conductivity of multivalent cation doped Li_6PS_5Cl solid electrolytes synthesized by mechanical milling, *RSC Advances* 10 (2020) 22304–22310.

[17] Hall, M.; Frank, E.; Holmes, G.; Pfahringer, B.; Reutemann, P.; Witten, I. H. The WEKA data mining software: an update. *ACM SIGKDD explorations newsletter*, 11(1) (2009) 10–18.

[18] Arganda-Carreras, I.; Kaynig, V.; Rueden, C.; Eliceiri, K. W.; Schindelin, J.; Cardona, A.; Sebastian Seung, H. Trainable Weka Segmentation: a machine learning tool for microscopy pixel classification, *Bioinformatics*, 33(15) (2017) 2424–2426.

[19] Lábár, J. L. Consistent indexing of a (set of) single crystal SAED pattern(s) with the ProcessDiffraction program, *Ultramicroscopy* 103 (2005) 237–249.

[20] Lábár, J. L. Electron diffraction based analysis of phase fractions and texture in nanocrystalline thin films, part I: Principles, *Microsc. Microanal.* 14 (2008) 287–295.

[21] Momma, K.; Izumi, F. VESTA 3 for three-dimensional visualization of crystal, volumetric and morphology data, *J. Appl. Crystallogr.* 44 (2011) 1272.

For Table of Contents Only